LUND UNIVERSITY

Accelerated Monte Carlo models to simulate fluorescence spectra from layered tissues

Swartling, Johannes; Pifferi, A; Enejder, AMK; Andersson-Engels, Stefan

[Link to publication]

Accelerated Monte Carlo models to simulate fluorescence spectra from layered tissues

Johannes Swartling

Lund University Medical Laser Centre, Department of Physics, Lund Institute of Technology, P.O. Box 118, SE-221 00 Lund, Sweden

Antonio Pifferi

Department of Physics, Politecnico di Milano, Piazza Leonardo da Vinci 32, I-20133 Milano, Italy

Annika M. K. Enejder

G. R. Harrison Spectroscopy Laboratory, Massachusetts Institute of Technology, 77 Massachusetts Avenue, Cambridge, Massachusetts 02139

Stefan Andersson-Engels

Lund University Medical Laser Centre, Department of Physics, Lund Institute of Technology, P.O. Box 118, SE-221 00 Lund, Sweden

Two efficient Monte Carlo models are described, facilitating predictions of complete time-resolved fluorescence spectra from a light-scattering and light-absorbing medium. These are compared with a third, conventional fluorescence Monte Carlo model in terms of accuracy, signal-to-noise statistics, and simulation time. The improved computation efficiency is achieved by means of a convolution technique, justified by the symmetry of the problem. Furthermore, the reciprocity principle for photon paths, employed in one of the accelerated models, is shown to simplify the computations of the distribution of the emitted fluorescence drastically. A so-called white Monte Carlo approach is finally suggested for efficient simulations of one excitation wavelength combined with a wide range of emission wavelengths. The fluorescence is simulated in a purely scattering medium, and the absorption properties are instead taken into account analytically afterward. This approach is applicable to the conventional model as well as to the two accelerated models. Essentially the same absolute values for the fluorescence integrated over the emitting surface and time are obtained for the three models within the accuracy of the simulations. The time-resolved and spatially resolved fluorescence exhibits a slight overestimation at short delay times close to the source corresponding to approximately two grid elements for the accelerated models, as a result of the discretization and the convolution. The improved efficiency is most prominent for the reverse-emission accelerated model, for which the simulation time can be reduced by up to two orders of magnitude. © 2003 Optical Society of America

OCIS codes: 170.6280, 170.3660, 170.7050, 300.6170.

1. INTRODUCTION

Fluorescence spectroscopy for medical applications is a diagnostic procedure under evaluation, attracting a growing interest.[1–3] This research has primarily addressed identification and localization of small lesions located superficially on the examined tissue. There has also been an interest in trying to measure the depth of such lesions as well as to locate lesions lying deep within the tissue by using laser-induced fluorescence.[4,5] The diagnostic applications based on this technique mainly depend on a discrimination in fluorescence properties between the lesion and the surrounding tissue. Such differences can be caused by spatial variations in fluorophore concentrations or alterations in the natural biochemical environment in the lesions of diagnostic interest. The fluorescence can also be generated by means of designer fluorescent probes that are normally quenched but inhibit their quenching

properties in a specific biochemical environment, such as that found in a cancer tumor.[6] However, it is well-known that the obtained fluorescence signals are not solely given by the properties of the fluorophore(s) studied but also depend on the optical properties of the examined tissue matrix. Migration of the excitation and emission photons through the tissue will disperse the fluorescence signal in time and space. Moreover, reabsorption of the emitted fluorescence inside the tissue will affect the fluorescence, resulting in a drastically different fluorescence detected compared with that intrinsically emitted. This effect has been problematic, e.g., in the case of fluorescence recordings intended for measurements of the concentration of a photosensitizer in tissue in conjunction with photodynamic therapy.[7]

Simple analytical models have been developed to extract the fluorophore concentrations from fluorescence measurements of tissue.[8–13] These models are designed

to correct for the dependence of reabsorption of the emitted fluorescence by relating the fluorescence signals to another recorded signal, e.g., the diffuse reflectance of the examined tissue at the fluorescence wavelength studied. Thus they do not require any knowledge of the exact optical properties of the tissue, since all information required on the tissue's optical properties is carried by the diffuse reflectance signal. The results show reasonable accuracy under certain conditions of measurement geometry and optical properties of the tissue examined. However, the methods often require careful calibration and fail to give accurate predictions when the assumptions are not fulfilled, e.g., when the fluorophore is not homogeneously distributed in the tissue. Another, more general approach to extract the intrinsic fluorescence information is to measure the optical properties of the tissue separately and correct the fluorescence recordings accordingly by using a theoretical model for light transport in tissue. This concept requires an accurate model for the generation and the propagation of fluorescence light in tissue. Several such models are suggested in the literature, among them diffusion theory[4,14,15] and various photon migration models.[12,16,17] They are all derived for restricted geometries, i.e., a homogeneous semi-infinite medium, or a set of optical properties of the tissue examined. A more general approach to modeling light propagation in turbid media without restrictions in geometry and optical properties is the method of Monte Carlo simulations.[18–21] It has been shown to provide accurate predictions of elastic light scattering in tissue and is thus often used as a gold standard to evaluate the accuracy of other models for light transport in tissue. Monte Carlo simulations provide several advantages compared with the above-mentioned methods. The method can handle complex geometries without restrictions in optical properties, which is not possible for analytical models. A unique feature is that the method directly can give information on where the light has traveled in the medium. This is difficult or impossible to obtain with other methods. These features make it possible to analyze how measured optical signals react to arbitrary changes in the optical properties of the medium. However, since it presents unique results for each specific light propagation problem without any simple analytical expressions for the distribution of light fluence, changing any of the input parameters requires a new simulation, resulting in long computation times. This is especially true for simulations of tissue fluorescence, since light is generated in a broad wavelength region, with each combination of excitation and emission wavelengths requiring an individual Monte Carlo simulation. The aim of this study is to develop efficient fluorescence Monte Carlo models, thereby making the Monte Carlo technique more feasible for applications within fluorescence spectroscopy of turbid media such as tissues. We consider not only steady-state fluorescence[22,23] but also the dimension of time, enabling simulations of time-resolved fluorescence. Furthermore, the advantages and the limitations of the accelerated models are evaluated by rigorous comparison with the well-tested conventional Monte Carlo approach in terms of accuracy and computation time required to achieve a predefined signal-to-noise ratio.

2. METHODS

The purpose of fluorescence Monte Carlo simulations is to study the process of fluorescence emission from a turbid medium containing a mixture of fluorophores of interest. Consider a short light pulse, at the excitation wavelength λ^x, entering the medium at normal incidence to the surface, as illustrated in Fig. 1. A simulated excitation photon path is then given by the propagation of a photon within the medium until it either escapes at the boundaries or is absorbed. When it is absorbed by a fluorophore, a new fluorescence photon is launched at the wavelength λ^m after a certain delay determined by the fluorescence lifetime of the fluorophore. The fluorescence photon propagates through the medium and is eventually absorbed or emitted at the surface. Reabsorption of the fluorescence photons by the fluorophore followed by secondary emission is neglected here. The optical properties of the medium at the excitation wavelength are described by the absorption coefficient μ_a^x, the scattering coefficient μ_s^x, and the anisotropy factor g^x. The absorption and scattering coefficients are defined as the probability of absorption and scattering per unit path length, respectively, and the anisotropy factor is defined as the mean cosine of the scattering angles. The Henyey–Greenstein phase function was utilized to sample the angular distribution of scattered photons in the simulations. The corresponding optical properties at the emission wavelength are described by μ_a^m, μ_s^m, and g^m. Furthermore, we introduce an effective quantum yield $\phi_{\text{eff}}(\lambda^x, \lambda^m, \Delta\lambda)$ that expresses the probability of a photon to be emitted within the wavelength range $\Delta\lambda$ at λ^m upon absorption of a photon at λ^x, with $\Delta\lambda \ll \lambda^m$. The effective quantum yield is derived from the intrinsic emission spectrum and the fraction of absorption events attributable to the fluorophore of interest (μ_a^{xf}/μ_a^x):

$$\phi_{\text{eff}}(\lambda^m) = \phi \, \frac{\mu_a^{xf}}{\mu_a^x} \, \frac{\eta(\lambda^m)\Delta\lambda}{\displaystyle\int_0^\infty \eta(\lambda)\mathrm{d}\lambda}, \tag{1}$$

where ϕ is the fluorescence quantum yield, μ_a^{xf} is the absorption coefficient of the fluorophore at the excitation wavelength, and $\eta(\lambda)$ is the spectral probability distribution of the generated fluorescence with respect to the
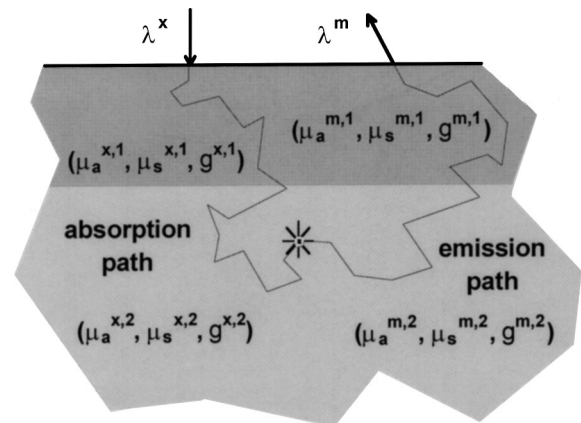

Fig. 1. The process of fluorescence emission from a multilayered semi-infinite turbid medium is schematically illustrated.

emission wavelength. The result of a simulation is given, for each emission wavelength λ^m, as the probability per unit area and time, $F(r, t)$, of fluorescence emission from the surface of the medium at the radial distance r from the injection point and after a time delay t. We have constructed three different models of fluorescence Monte Carlo simulations. In the conventional method, each individual photon is traced from its excitation state through a possible launch of a fluorescence photon to a subsequent emission state. In contrast, what we call the forward- and reverse-emission methods are based on convolution of the absorption distribution of the excitation light with the emission distribution of the fluorescence light. Moreover, the so-called white Monte Carlo (WMC) approach[24–26] has been employed. This concept permits analytical computations of the light transport in tissue for any absorption coefficient based on the results from a single simulation of a nonabsorbing medium, provided that the scattering and geometrical properties remain the same.

A. Standard Fluorescence Monte Carlo Method

A conventional or standard fluorescence Monte Carlo (SMC) model was developed, essentially following the concepts outlined by Welch *et al.*[20,21] In addition, our model provides not only spatial but also temporal information on the fluorescence. In contrast to the fixed-weight photon model used by Welch *et al.*, a quasi-weighted photon model is employed in this work; i.e., the weight of the excitation photon is decreased at each interaction site and inherited by the fluorescence photon. However, no major differences in obtained accuracy between the two alternatives are reported.[20,21] Basically, the SMC method consists of three parts, as illustrated in Fig. 1. The first part involves a SMC simulation, based on the computation routines of Wang *et al.*,[27] at the excitation wavelength with the corresponding optical properties. A fluorescence photon may then be generated at a certain probability and time delay. The third part consists again of a SMC simulation, but now at the emission wavelength and consequently with the corresponding optical properties.

B. Convolution and the Forward-Emission Monte Carlo Method

A more efficient fluorescence simulation procedure can be devised by exploiting the symmetry properties of the problem. The geometry of the problem is restricted to a multilayered structure infinite in the radial dimension as shown in Fig. 2(a); i.e., we assume that the medium is composed of adjacent slabs of different thicknesses and optical properties. We use a cylindrical coordinate system (r, φ, z), centered at the injection point of the excitation light, with the time delay t as a fourth coordinate. The fluorescence process can be split into three separate events, which we recognize from the SMC method. These three events are depicted in Fig. 1: (1) propagation of the excitation photon, (2) isotropic emission of a photon after a certain delay, and (3) propagation of the emitted photon. The intention with this approach is to model each process with a complete set of photons separately and derive the final result by combining the individual re-
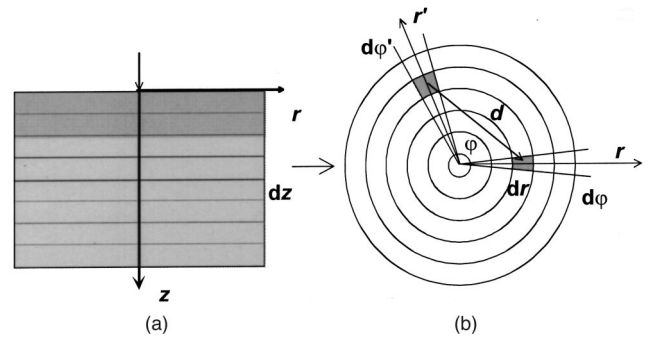

Fig. 2. Geometry used for the simulations. (a) The medium is divided into volume elements using a grid along the r and z axes. Similarly, time is divided into dt intervals. (b) View of the coordinate system used to calculate the convolution for a slab of thickness dz.

sults afterward.[28] A similar approach was used by Avrillier *et al.* for steady-state problems.[23]

We can describe the absorption probability of the excitation light by using the quantity $A(r, t, z)$, defined as the probability per unit volume and time for an excitation photon to be absorbed at a radial distance r, a depth z, and a delay t from the injection point. This quantity can be calculated from one single Monte Carlo simulation based on the optical properties for the excitation wavelength. Moreover, an emission probability $E(r, t, z)$ can be defined as the probability per unit area and time to detect a fluorescence photon originating from the depth z at the radial distance r from the fluorescence emission point after the delay t. This matrix can be obtained separately from Monte Carlo simulations by an isotropic launch of photons at the depth z within the medium with the optical properties for the emission wavelength. This means that one simulation has to be conducted for each depth z of interest. Finally, $D(t)$ is the time decay of the fluorescence emission. For a single-exponential time decay,

$$D(t) = \frac{1}{\tau} \exp\left(-\frac{t}{\tau}\right) \tag{2}$$

is applicable, where τ is the lifetime of the fluorophore.

These three quantities, i.e., $A(r, t, z)$, $E(r, t, z)$, and $D(t)$, are all linear with respect to the number of simulated photons when neglecting all nonlinear interactions. Moreover, each is invariant with respect to the initialization time t_0 for the process, where in the (r, φ) plane the process starts with an infinite, layered structure assumed. Thus it is possible to apply the method of convolution for both the temporal and radial variables. Since the z direction is not space invariant, only the superposition principle and not convolution can be applied along this axis.

For simplicity, we start by considering the case of instantaneous fluorescence emission ($\tau = 0$). We can then calculate the probability $F_z^{inst}(r, t, z)dz$ for a fluorescence photon generated in dz at the fixed depth z to escape the surface of the medium. It can be done by convolving the probabilities $A(r, t, z)$ and $E(r, t, z)$ in time and space, weighting for the effective quantum yield [Fig. 2(b)]:

$$F_z^{\text{inst}}(r, t, z)\mathrm{d}z = \mathrm{d}z \int_0^\infty r'\mathrm{d}r' \int_0^{2\pi} \mathrm{d}\varphi' \int_0^\infty \phi_{\text{eff}} A(r', t', z)$$

$$\times E(d, t' - t, z)\mathrm{d}t', \tag{3}$$

where $d = (r^2 + r'^2 + 2rr'\cos\varphi')^{1/2}$. Then we sum all the contributions $F_z^{\text{inst}}(r, t, z)\mathrm{d}z$ along the z axis:

$$F^{\text{inst}}(r, t) = \int_0^\infty F_z^{\text{inst}}(r, t, z)\mathrm{d}z. \tag{4}$$

Finally, the decay profile of the fluorescence emission is taken into account by convolving $F^{\text{inst}}(r, t)$ with $D(t)$:

$$F(r, t) = \int_0^\infty F^{\text{inst}}(r, t')D(t' - t)\mathrm{d}t'. \tag{5}$$

Whereas the absorption probability distribution $A(r, t, z)$ can be determined from a single Monte Carlo simulation based on the optical properties of the excitation light, the emission probability distribution $E(r, t, z)$ requires one simulation for each depth z. In practice, $E(r, t, z)$ is obtained by randomly choosing the depth z_s of the source for every launched photon in a single Monte Carlo simulation and classifying the emitted photons according to the z_s value. The benefit of the convolution method is that it will reduce the need for good photon statistics, and thus the computation time, due to the integration over the r, φ, and t coordinates. We call this approach the forward-emission Monte Carlo (FMC) method.

C. Reverse-Emission Monte Carlo Method

To reduce the number of Monte Carlo simulations required to calculate the emission probability, a methodology to obtain $E(r, t, z)$ by a single reverse-emission simulation was developed as illustrated in Fig. 3. Instead of launching the fluorescence photons at different depths z within the medium [Fig. 3(a)] and recording the number of collected photons at the surface, one can set a source at the surface of the medium and record the spa-

Fig. 3. The concepts of (a) forward Monte Carlo (FMC) and (b) reverse Monte Carlo (RMC) methods are illustrated. The tissue surface is along the r axis, and $\mathbf{n}$ is the normal vector. In (a), an isotropic point source at S_1 is considered, corresponding to fluorescence emission from this point. The radiant flux across the surface boundary is measured at D_1. In (b), a point source at S_2 is assumed. The fluence rate is measured at D_2. The gray line represents one possible photon trajectory between the two points. The cone $\Delta\Omega$ at D_1 and at S_2 represents the solid angle of acceptance for emission at the surface, defined by the condition for total reflection. Furthermore, $\mathbf{r}_{S2} = \mathbf{r}_{D1}$ and $\mathbf{r}_{D2} = \mathbf{r}_{S1}$.

tial and temporal distributions of the absorbed photons [Fig. 3(b)]. The intention of this reverse-path method is to better utilize the photons simulated with the Monte Carlo technique. In a forward-path simulation, useful information related to the photon path is recorded only when the photons exit the medium. Since photons that are terminated after several interaction events within the medium are lost photons in this respect, more than one photon path is needed on average to generate useful information. In a reverse-path simulation, information is instead stored at the many more individual interaction sites along each photon path. Except for a scaling factor, the emission probability $E(r, t, z)$ is then given by the absorption probability $A_{\text{rev}}(r, t, z)$, obtained from a single Monte Carlo simulation based on the optical properties for the emission wavelength. This approach was followed by Crilly *et al.*[22] for steady-state fluorescence, but without a derivation of the scaling factor coupling the forward and reverse computations. Instead, they relied on empirical determination by comparing with results generated by forward computations. Here we derive the scaling factor by means of the reciprocity theorem.[29,30] Let us set up the definitions needed for this derivation.

In the forward case, an isotropic source emits fluorescence light at a depth z. At the point $(r, 0)$ on the surface with the radial distance r from the source, fluorescence photons may escape provided that their angle of incidence is smaller than the critical angle for total reflection. Now consider the reciprocal situation modeled by the reverse-path computations, where fluorescence light is injected at the surface at $(0,0)$ and absorbed in a point (r, z). The fluence rate absorbed here must consequently correspond to the light flux emitted at the surface in the forward computations, originating from an isotropic light source in (r, z), for one to be able to employ the more efficient reverse approach. The two situations, forward and reverse, are depicted in Fig. 3 with their intrinsic coordinate systems interrelated by a translation along the radial axis. For clarity, a common coordinate system is defined with its origin located at O'. The detection and source sites in the forward (reverse) case are referred to as D_1 and (D_2) and S_1 (S_2). In the forward case, let $L(\mathbf{r}_{D1}, \mathbf{s})$ be the radiance at D_1, given in power per unit area and solid angle, in the direction $\mathbf{s}$. The net radiant flux that escapes across the boundary at the surface at D_1 due to the source at S_1 is then defined as

$$\text{FWD}(\mathbf{r}_{D1}) = \int_{\Delta\Omega} L(\mathbf{r}_{D1}, -\mathbf{s})[1 - R(|-\mathbf{s} \cdot \mathbf{n}|)]$$

$$\times (-\mathbf{s} \cdot \mathbf{n})\mathrm{d}\Omega(\mathbf{s}). \tag{6}$$

The quantity $R(|\mathbf{s} \cdot \mathbf{n}|)$ is the Fresnel reflection coefficient of light incident in the direction $\mathbf{s}$ at the interface, defined by

$$R(\theta_2) = \frac{1}{2}\left[\frac{\sin^2(\theta_2 - \theta_1)}{\sin^2(\theta_2 + \theta_1)} + \frac{\tan^2(\theta_2 - \theta_1)}{\tan^2(\theta_2 + \theta_1)}\right],$$

$$\theta_2 = \cos^{-1}(|\mathbf{s} \cdot \mathbf{n}|), \qquad n_1\sin\theta_1 = n_2\sin\theta_2. \tag{7}$$

The integral is taken over the solid angle $\Delta\Omega$ defined by the critical angle for total reflection. Note the negative
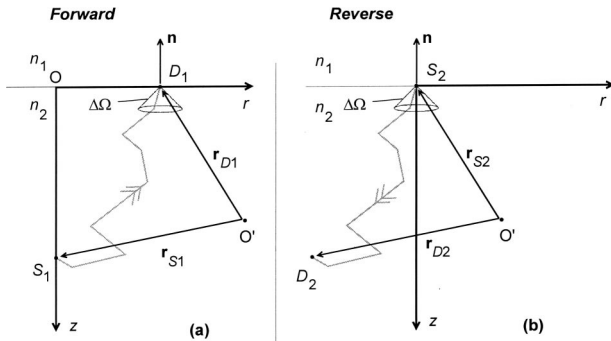
sign on the directional vector **s**, because **s** is directed inward, toward the medium, when taken over $\Delta\Omega$, while the integral over L should be performed outward from the medium. Similarly, let $L(\mathbf{r}_{D2}, \mathbf{s})$ be the radiance at D_2 in the direction **s** in the reverse case. The fluence rate at D_2 due to a source at S_2 is then defined as

$$\text{REV}(\mathbf{r}_{D2}) = \int_{4\pi} L(\mathbf{r}_{D2}, \mathbf{s}) d\Omega(\mathbf{s}). \quad (8)$$

Let $L_1(\mathbf{r}, \mathbf{s})$ be the radiance generated by a source $Q_1(\mathbf{r}, \mathbf{s})$ and $L_2(\mathbf{r}, \mathbf{s})$ be that of a source $Q_2(\mathbf{r}, \mathbf{s})$. The sources $Q_1(\mathbf{r}, \mathbf{s})$ and $Q_2(\mathbf{r}, \mathbf{s})$ are given in units of intensity, power per unit solid angle. Provided that the phase function [$p(\mathbf{s}, \mathbf{s}')$, i.e., the probability that a photon propagating in the direction **s** is scattered into the direction **s**'] is invariant under time reversal, and that there are no other light sources, it can be shown that[29,30]

$$\int\int_{4\pi} L_2(\mathbf{r}, \mathbf{s}) Q_1(\mathbf{r}, -\mathbf{s}) d\Omega(\mathbf{s}) dV$$

$$= \int\int_{4\pi} L_1(\mathbf{r}, -\mathbf{s}) Q_2(\mathbf{r}, \mathbf{s}) d\Omega(\mathbf{s}) dV. \quad (9)$$

This is the integral version of the reciprocity theorem. Now consider the specific case in Fig. 3. The point sources $Q_1(\mathbf{r}, \mathbf{s})$ for the forward case and $Q_2(\mathbf{r}, \mathbf{s})$ for the reverse case may be written as

$$Q_1(\mathbf{r}, \mathbf{s}) = \frac{P_{\text{fwd}}}{4\pi} \delta(\mathbf{r} - \mathbf{r}_{S1}), \quad (10)$$

$$Q_2(\mathbf{r}, \mathbf{s})$$

$$= \begin{cases} \dfrac{P_{\text{rev}}}{\Delta\Omega}[1 - R(|\mathbf{s} \cdot \mathbf{n}|)](\mathbf{s} \cdot -\mathbf{n}) \delta(\mathbf{r} - \mathbf{r}_{S2}) \\ \qquad \text{if } \mathbf{s} \text{ is inside } \Delta\Omega \\ 0 \qquad \text{if } \mathbf{s} \text{ is not inside } \Delta\Omega \end{cases},$$

$$(11)$$

where P_{fwd} and P_{rev} are the powers emitted by the sources. Starting with the left-hand side (LHS) of Eq. (9), we have, after inserting Eq. (10),

$$\text{LHS} = \int\int_{4\pi} L_2(\mathbf{r}, \mathbf{s}) \frac{P_{\text{fwd}}}{4\pi} \delta(\mathbf{r} - \mathbf{r}_{S1}) d\Omega(\mathbf{s}) dV$$

$$= \frac{P_{\text{fwd}}}{4\pi} \int_{4\pi} L_2(\mathbf{r}_{S1}, \mathbf{s}) d\Omega(\mathbf{s}). \quad (12)$$

Since, according to Fig. 3, $\mathbf{r}_{S1} = \mathbf{r}_{D2}$, the last integral in Eq. (12) is equal to $\text{REV}(\mathbf{r}_{D2})$ [Eq. (8)]. Similarly, for the right-hand side (RHS), we have

$$\text{RHS} = \int\int_{4\pi} L_1(\mathbf{r}, -\mathbf{s}) \frac{P_{\text{rev}}}{\Delta\Omega}[1 - R(|\mathbf{s} \cdot \mathbf{n}|)](\mathbf{s} \cdot -\mathbf{n})$$

$$\times \left. \delta(\mathbf{r} - \mathbf{r}_{S2}) \right|_{\mathbf{s} \in \Delta\Omega} d\Omega(\mathbf{s}) dV$$

$$= \frac{P_{\text{rev}}}{\Delta\Omega} \int_{\Delta\Omega} L_1(\mathbf{r}_{S2}, -\mathbf{s})[1 - R(|\mathbf{s} \cdot \mathbf{n}|)]$$

$$\times (\mathbf{s} \cdot -\mathbf{n}) d\Omega(\mathbf{s}). \quad (13)$$

Since $\mathbf{r}_{S2} = \mathbf{r}_{D1}$, the last integral is equal to $\text{FWD}(\mathbf{r}_{D2})$. The result is that

$$\text{REV}(\mathbf{r}_{D2}) = \frac{P_{\text{rev}}}{P_{\text{fwd}}} \frac{4\pi}{\Delta\Omega} \text{FWD}(\mathbf{r}_{D1}). \quad (14)$$

Hence, for the reverse, or reciprocal, case, the incident power should be chosen as

$$P_{\text{rev}} = \frac{\Delta\Omega}{4\pi} P_{\text{fwd}} \quad (15)$$

to yield a result equal to that in the forward case. In practice, the source $Q_2(\mathbf{r}, \mathbf{s})$ can readily be implemented in the Monte Carlo simulation with a restraint, corresponding to $\Delta\Omega$, in the angles of the incident photons allowed to continue within the medium. In addition, the absorption probability distribution $A_{\text{rev}}(r, t, z)$ must be scaled with the factor $4\pi/\Delta\Omega$ in order to be used as an emission probability distribution. The presence of multiple layers with different refractive indices does not impose any problem, since such interfaces also obey invariance under time reversal. We call this approach the reverse-emission Monte Carlo (RMC) method.

D.   White Monte Carlo Approach

All the above-mentioned fluorescence Monte Carlo methods (standard, forward emission, and reverse emission) require one emission probability [$E(r, t, z)$] simulation for each emission wavelength of interest, since the optical properties depend on the wavelength. Moreover, the fluorophore itself can absorb the emitted photons depending on its wavelength, and μ_a^m must be altered accordingly. One way to reduce the number of simulations required is to utilize the white Monte Carlo (WMC) technique.[23–26] This approach can be useful in simulating different emission wavelengths, fluorophore concentrations, and background absorptions starting from a single Monte Carlo simulation with the fluorescence absorption set to zero ($\mu_a^m = 0$). The results are instead analytically scaled for the absorption afterward, which is easily repeatable for a list of absorption coefficients. This approach is motivated by the fact that the photon path in the medium is essentially determined by the scattering properties (μ_s, g) only, while the absorption coefficient in general determines the survival probability of every possible photon path. If the time t_i spent by every simulated photon in each layer i is recorded as a measure of the effective path length, it is possible to reconstruct the distribution $E(r, t, z)$ for the set of absorption coefficients of interest by simply weighting the total photon

path in each layer obtained from the null-absorption simulation with a Beer–Lambert factor:

$$w = \prod_{i=1}^{nl} \exp\left(\frac{-\mu_a^{m,j} c t_i}{n_i}\right), \qquad (16)$$

where n_i is the refractive index of the ith layer and the index i runs over all nl layers. One limitation, however, somewhat restricting the full utilization of the method to derive a full fluorescence emission spectrum, is that the scattering properties must remain the same. This is usually the case if the wavelength range is small (e.g., $\Delta\lambda < 50$ nm). For wider spectral ranges, one should perform a set of separate simulations splitting the whole range into smaller regions where the scattering is reasonably constant. This problem can be overcome completely if the medium can be regarded as homogeneous, since then a rescaling of the spatial scale is equivalent to rescaling the scattering coefficient.[23] The WMC concept is fully compatible with transport theory and has previously been shown to provide accurate results.[24] No systematic analysis of its accuracy will therefore be presented here.

E. Code Implementation and Simulations

The Monte Carlo code written by Wang *et al.*,[27] including temporal resolution added by Berg,[31] was modified to support the different approaches described in Subsection 2.D. It was written in C and run on Pentium III processors. The launch of fluorescence photons was added in the standard Monte Carlo (SMC) method, and the convolution was combined with the forward-emission (FMC) or the reverse-emission (RMC) concept in the accelerated methods. In the convolution in Eq. (3), the integration over time and space should be performed to infinity. In the numerical convolution, the integrals were evaluated over finite grids that represent the distributions $A(r, t, z)$ and $E(r, t, z)$. This means that the outer bounds of the grids were set at the point where the signal level outside the grid was so low that it could be neglected. The White Monte Carlo approach (WMC) can be implemented in any of the three simulation methods; however, the data shown here were obtained from the FMC method. The FMC program was designed with an option to set μ_a^m to zero and track the path length of the fluorescence photons per layer, followed by a scaling with the Beer–Lambert factor according to Eq. (16).

The SMC approach was in this study used as a gold standard. Thus the results obtained with the convolution approach using either the FMC method for the calculation of the emission matrix or the RMC method were compared with those from the SMC method. Differences in spatial/temporal distributions of the fluorescence probability were analyzed and given in relative numbers. All simulations were done by using the simplest possible geometry, a semi-infinite homogeneous medium. Values used as input parameters, unless stated differently, are defined in Table 1. This set of data contains absorption and scattering parameters typical for tissue. It formed a reference simulation when various aspects were to be considered, in order to evaluate the performance and the accuracy of the accelerated methods. The time required for such a reference simulation run with 100,000 photons was compared for the four methods, including the FMC method with the WMC approach, as a measure of computation efficiency. To evaluate the sensitivity to changes in the optical properties, we conducted a series of simulations, each with 100,000 photons launched, where each parameter from the reference simulation was varied in turn. The values of the altered parameters are listed in Table 2. Furthermore, the influence of grid size used in the derivation of the distributions $A(r, t, z)$, $E(r, t, z)$ and $F(r, t, z)$ was investigated in the time domain by repeating the reference simulation with dt set not only to 5 ps but also to 1 ps. Finally, the statistics of the results with respect to the number of launched photons were evaluated by repeating the reference simulation five times. This was conducted for six levels of statistics, the lowest corresponding to the launch of 1000 photons and the highest to 1,024,000 photons.

F. Evaluation Criteria

Various parameters were calculated to compare the performance and the accuracy of the different methods. A measure of the total probability of detecting a fluorescence photon escaping the surface of the medium is defined as

$$F_{\text{TOT}} = \int_0^\infty 2\pi r \, dr \int_0^\infty F(r, t) \, dt \qquad (17)$$

and is computed as the number of fluorescence photons at the surface divided by the number of initially launched excitation photons. A second quantity evaluated is the radial distribution of the fluorescence probability, obtained by integrating the emitted fluorescence in time:

$$F_{\text{CW}}(r) = \int_0^\infty F(r, t) \, dt. \qquad (18)$$

It is given as the number of escaping fluorescence photons per launched excitation photon and unit area. A third function compared in this study is the time distribution for a series of fixed radial positions $\bar{r}$:

$$F_{\bar{r}}(t) = F(\bar{r}, t), \qquad (19)$$

Table 1. Standard Values of Input Parameters Used in the Simulations

Optical Properties							Grid Resolution				Grid Size		
μ_a^x (cm^{-1})	μ_a^m (cm^{-1})	μ_s^x (cm^{-1})	μ_s^m (cm^{-1})	g^x	g^m	ϕ_{eff}	τ (ps)	dz (cm)	dr (cm)	dt (ps)	nz	nr	nt
2.0	0.5	100	50	0.8	0.84	0.25	1	0.025	0.05	5	20	40	40

Table 2. Values of F_{TOT} Obtained for Different Optical Properties[a]

Changed Parameters	Model	F_{TOT}	DF_{TOT} (%)
None	SMC	0.0157	
	FMC	0.0161	2.3
	RMC	0.0162	3.0
$\mu_a{}^x = 1.0 \text{ cm}^{-1}$	SMC	0.0122	
	FMC	0.0123	0.9
	RMC	0.0123	1.5
$\mu_a{}^m = 0.25 \text{ cm}^{-1}$	SMC	0.0193	
	FMC	0.0193	0.0
	RMC	0.0196	1.2
$\mu_s{}^x = 50 \text{ cm}^{-1}$	SMC	0.0160	
	FMC	0.0165	3.0
	RMC	0.0166	3.6
$\mu_s{}^m = 100 \text{ cm}^{-1}$	SMC	0.0171	
	FMC	0.0176	3.0
	RMC	0.0176	2.9
$g^x = 0.7, g^m = 0.76$	SMC	0.0161	
	FMC	0.0161	0.5
	RMC	0.0165	2.6

[a] The values of F_{TOT} are presented in units of (detected fluorescence photons)/(injected excitation photons). The column DF_{TOT} expresses the relative difference between F_{TOT} and the value obtained with the SMC model. If not otherwise stated, the simulation parameters were those shown in Table 1.

given as fluorescence probability per unit time and unit area. In addition, the coefficient of variation (CV) was calculated for all fluorescence-probability parameters defined in Eqs. (17)–(19), based on five independent simulations run under identical conditions. These indices of statistical variability quantify the stability of each of the three methods. From the standard deviations $\sigma_i(r_i, t_i)$ of the parameters F_{TOT}, $F_{\text{CW}}(r_i)$, $F_{10\%}(r_i, t_i)$, $F_{1\%}(r_i, t_i)$, and $F_{0.1\%}(r_i, t_i)$, corresponding coefficients of variation were derived from

$$\text{CV} = \frac{1}{N} \sum_i \frac{|\sigma_i(r_i, t_i)|}{F(r_i, t_i)}, \tag{20}$$

where the index i runs over all N points in the (r, t) space of the selected region. $F_{10\%}(r_i, t_i)$, $F_{1\%}(r_i, t_i)$, and $F_{0.1\%}(r_i, t_i)$ correspond to the fluorescence-probability distributions truncated for values less than 10%, 1%, and 0.1% of the maximum $F(r_i, t_i)$ value.

G. Demonstration of a Simulated Fluorescence Spectrum

To demonstrate the efficiency of the accelerated models, we will give an example based on a possible realistic application. During a photodynamic therapy treatment, a photosensitizing agent is first administered to the tumor region and is then used in a photoinduced chemical reaction to kill the cancer cells. One problem when controlling the process is knowing the concentration of sensitizer in the tissue, since this is a complex function of the rates of uptake and metabolism and also of the rate of photobleaching by the excitation light. A common photosensitizer is protoporphyrin-IX (PpIX), which is excited at

635 nm. PpIX fluorescence excited by 635-nm light occurs predominantly in the 705-nm band.

A model was simulated as a twin-layered structure, where the top 5 mm had optical properties typical of those of skin and the lower layer had properties like those of fatty tissue. Three stages were simulated, which would mimic the photobleaching process. To start, we impregnated the top 3-mm layer with PpIX. In the next stage, PpIX was removed from the top 1-mm layer, leaving a 2-mm layer of PpIX underneath. In the last stage, only a 1-mm-thick layer of PpIX at a depth of 2 mm remained. Thus the photobleaching process was approximated by removing layers of PpIX from the top downward in two steps.

3. SIMULATION RESULTS

As a first example of the output of the reference simulation obtained with the different methods, Fig. 4 shows the full $F(r, t)$ distribution obtained with the SMC [Fig. 4(a)], FMC [Fig. 4(b)], and RMC [Fig. 4(c)] methods, respectively. The input parameters used in the simulations were those defined in Table 1. The number of launched photons was 10^6 for the SMC method and 10^5 for both the FMC and RMC methods. The shapes of the distributions obtained from the three different simulations are clearly similar. The results from the RMC simulation are quite smooth, and the distribution obtained from the FMC simulation exhibits comparable noise level with that obtained from the SMC simulation, even though the number of photons used in the accelerated simulations was only 1/10 of that in the standard method. To evaluate the accuracy of the methods in more detail, and thereby able to better appreciate limitations and advantages of the different approaches, we have evaluated the methods by using the parameters defined above. The total fluorescence probability intensity F_{TOT} for different optical properties is presented in Table 2. The accelerated methods yield slightly overestimated values of F_{TOT} as compared with the SMC method irrespective of the optical properties. The discrepancy is on average approximately 2.5% for the RMC method and 1.5% for the FMC method, which is of the same order as the uncertainty due to the stochastic nature of the simulation method, however systematic. This systematic discrepancy between the accelerated models and the conventional method is due to the temporal discretization of the grid and originates from an overestimation of the fluorescence for very early times. The error was reduced if smaller time grid elements were employed (cf. the results in Fig. 7, discussed below).

Radial distributions of the corresponding simulations, F_{CW}, are shown in Fig. 5, i.e., for the values given in Table 1 in Fig. 5(a), for $\mu_a{}^x$ reduced to 1.0 cm^{-1} in Fig. 5(b), for $\mu_a{}^m$ reduced to 0.25 cm^{-1} in Fig. 5(c), for $\mu_s{}^x$ reduced to 50 cm^{-1} in Fig. 5(d), for $\mu_s{}^m$ increased to 100 cm^{-1} in Fig. 5(e), and, finally, for g^x and g^m reduced to 0.7 and 0.76, respectively, in Fig. 5(f). In general, there is good agreement among the three methods for all optical properties, although the intensities deviate slightly at larger distances ($r > 0.7$ cm) from the incident beam.
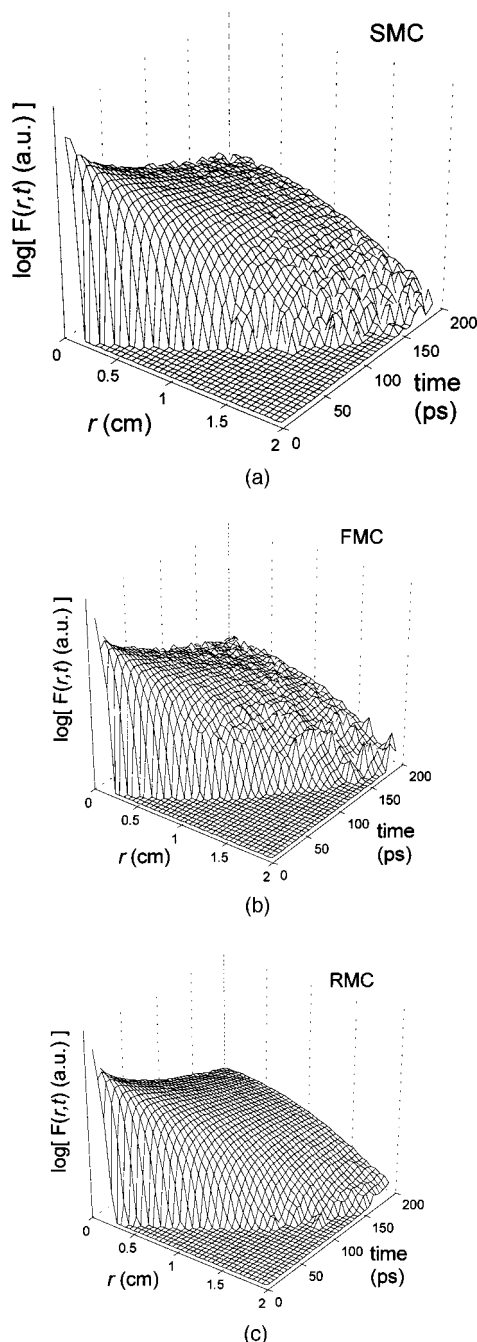
SMC

(a)

FMC

(b)

RMC

(c)

Fig. 4.   Examples of results obtained from simulations using the reference parameters listed in Table 1 when employing the (a) SMC, (b) FMC, and (c) RMC methods.   A total number of 10^6 photons was used for the SMC method, yielding a computation time of 13 min on a Pentium III 933-MHz processor.   For the FMC and RMC methods, 10^5 photons were used, and the corresponding computation times were 77 and 75 s, respectively.

This deviation is due to the truncated grid over which the convolution is performed.   The numerical convolution assumes that absorption and emission distributions are zero beyond the grid boundary, which leads to underestimated fluorescence close to the grid boundary.

A comparison of the models in the time domain is made for $\bar{r} = 0.05$ cm in Figs. 6(a)–6(c) and for $\bar{r} = 0.5$ cm in Figs. 6(d)–6(f).   The first set [Figs. 6(a) and 6(d)] shows the curves obtained from the reference simulation.   In

the second set [Figs. 6(b) and 6(e)], $\mu_a{}^m$ was reduced to 0.25 cm^{-1}, and in the third set [Figs. 6(c) and 6(f)] $\mu_s{}^m$ was increased to 100 cm^{-1}.   The agreement among the results from all three methods is good, with some discrepancy notable at the first two grid elements (d$t = 5$ ps, $\tau = 1$ ps).   When the time spacing is reduced from 5 ps down to 1 ps, there is better agreement among the methods even at early times, as shown in Fig. 7.   This indicates that a finer grid spacing yields better results, but at the expense of longer simulation time.   Similar conclusions hold for the other combinations of optical properties listed in Table 2 (data not shown).

The next aspect to be considered is the time required to obtain sufficient simulation photon statistics.   Table 3 reports the computer time registered for the different simulation processes, all run on a Pentium III 933-MHz processor.   Both the FMC and RMC methods employ the convolution stage, introducing a fixed computation time, independent of the number of simulated photons.   The number of operations of the convolution roughly scales as $(nt)^2(nr)^3nz$, where nt, nr, and nz are the number of grid elements in the t, r, and z axis, respectively.   To be able to separate the influence of number of photons and grid elements, we list the convolution time separately.   A simulation utilizing the WMC approach, here implemented in the FMC method, will take longer, since it is performed with $\mu_a{}^m = 0$, leading to a higher survival time for the simulated photons.   Nonetheless, this overhead is rapidly compensated for in the case of multiple simulations with different values of $\mu_a{}^m$, since the time required to apply the Beer–Lambert factor in the WMC model is negligible compared with the time required to simulate the $E(z, r, t)$ matrix.

The evaluation of the photon statistics of the simulations is based on the coefficient of variation [CV, Eq. (20)], derived from five repeated reference simulations.   Table 4 presents the CV values for the total and radial fluorescence probabilities, as well as for the entire spatial and temporal fluorescence distribution, truncated at three different relative thresholds.   Clearly, the best signal-to-noise ratio is obtained with the RMC method, followed by those from the FMC and SMC methods.

For the demonstration of fluorescence from PpIX, excited by 635-nm light, optical properties used for the tissue approximately corresponded to those given in Ref. 32 for the various tissues.   The shapes of the absorption spectra were determined by the absorption of water, fat, and hemoglobin.   The scattering coefficients decreased slightly toward longer wavelengths.   The grid parameters were the same as those used for the other simulations.   Simulations were carried out in the region 640–800 nm every 10 nm, totaling 16 simulations for all wavelength bands.   For the SMC computation, one simulation using 10^6 photons was performed for each wavelength band and each of the three stages of photobleaching, yielding a total of 48 simulation runs.   The computation time was 24 h per spectrum on a Pentium III 933-MHz computer.   Thanks to the convolution technique, only $3 + 16$ simulation runs had to be performed for the accelerated models.   In each run, 10^5 photons were launched.   The computation time including convolution was 20 min for the first spectrum, but since the
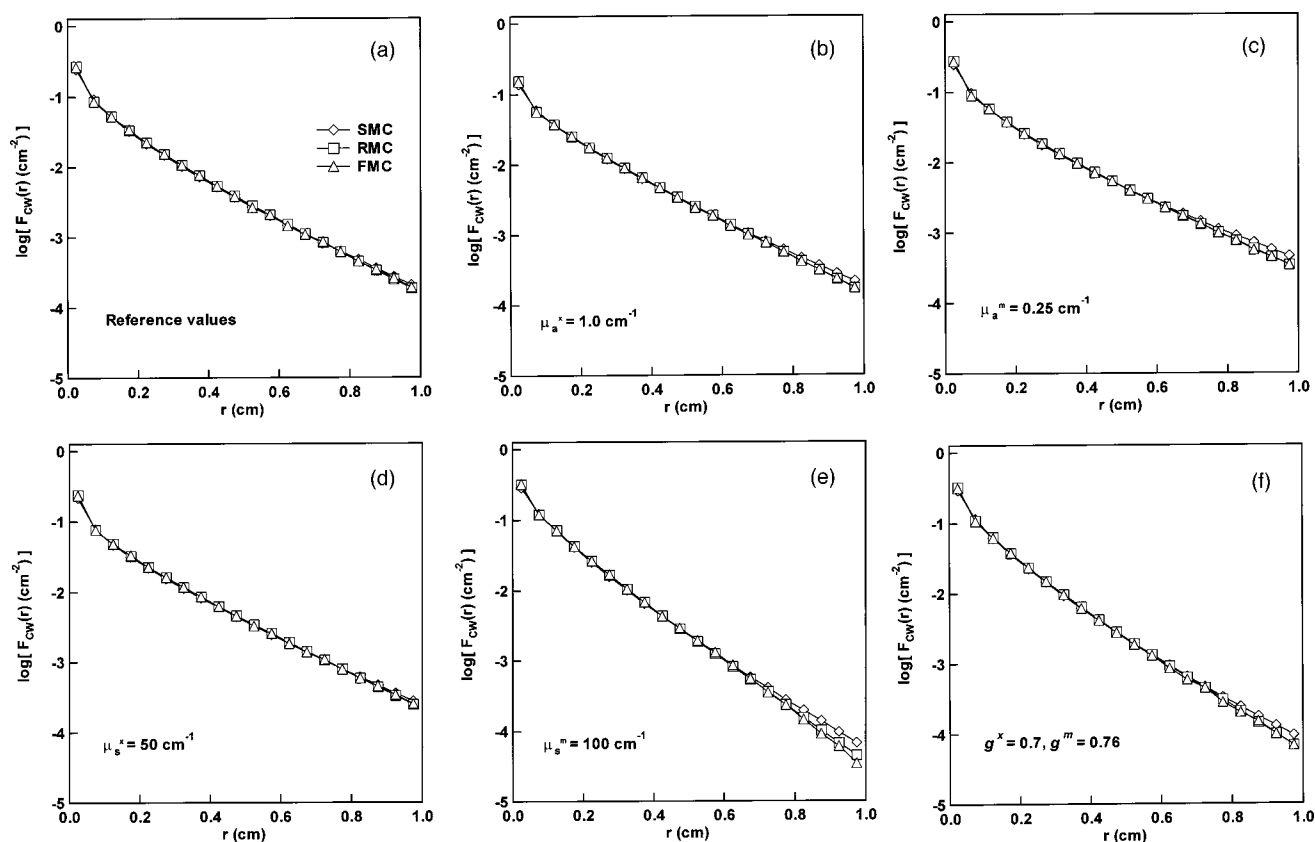
Fig. 5.   Plots of $F_{CW}(r)$ are shown, obtained from SMC (diamonds), RMC (squares), and FMC (triangles) simulations.   The simulation conditions are the reference values listed in Table 1 if not otherwise stated.

Fig. 6. $F_r(t)$ is shown for (a)–(c) $r = 0.05$ cm and (d)–(f) $r = 0.5$ cm plotted versus time.   The results are obtained from SMC (diamonds), RMC (squares), and FMC (triangles) simulations.   The simulation conditions are again the reference values listed in Table 1 if not otherwise stated.
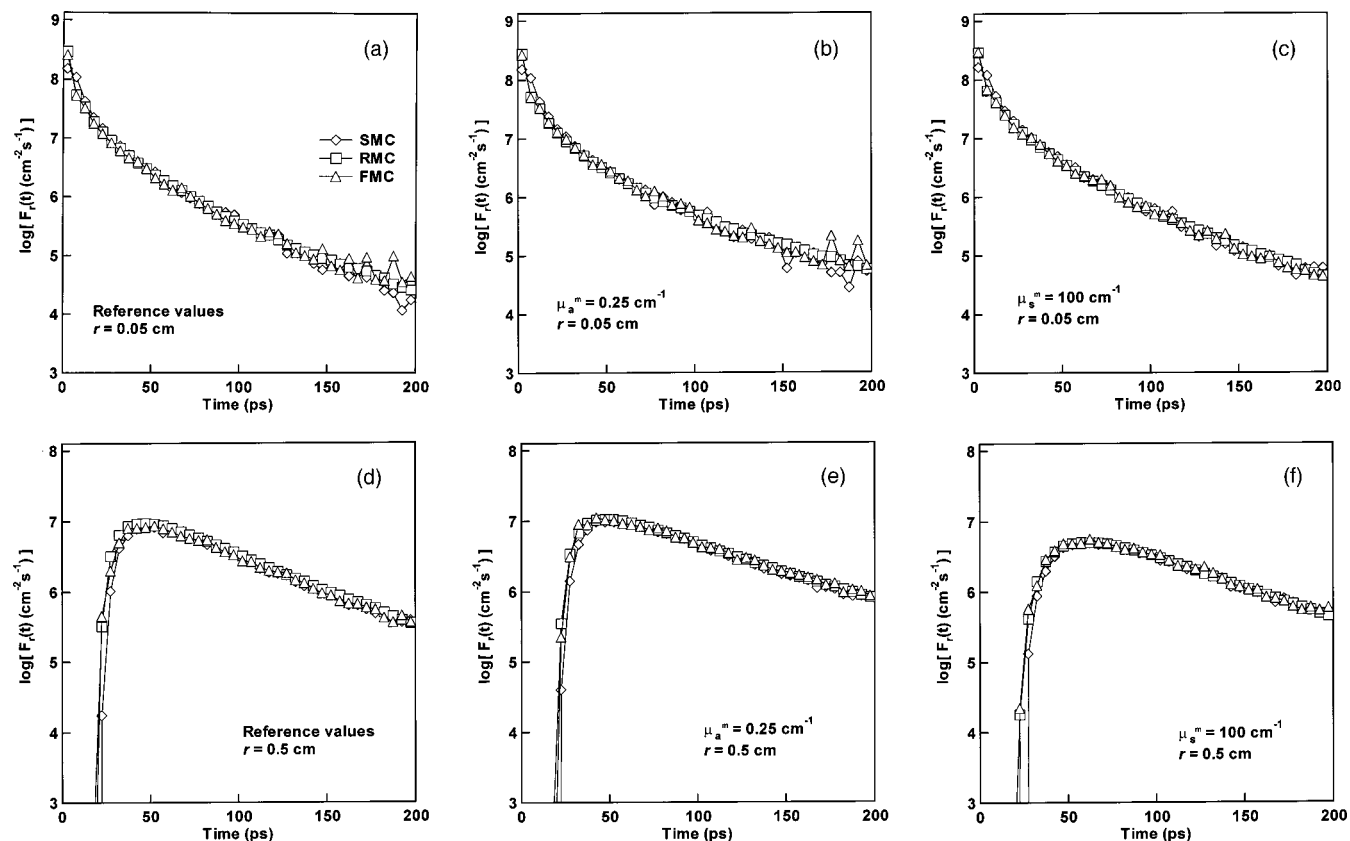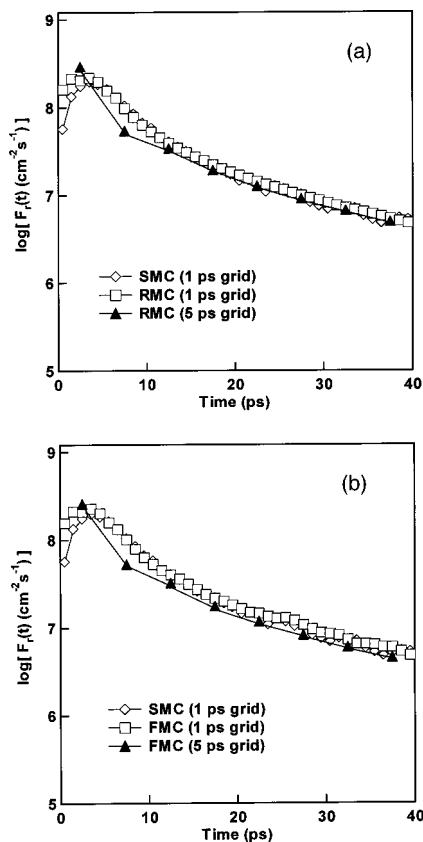
Fig. 7. Data derived from SMC simulations are compared with results obtained from (a) RMC and (b) FMC simulations, with respect to the size of the time grid element ($r = 0.05$ cm, and optical properties are as defined in Table 1).

Table 3. Computation Time for the Different Models

Method	Run Time on a Pentium III at 933 MHz (s)
SMC (10^5 photons)	78
FMC (10^5 photons)[a]	58
RMC (10^5 photons)[a]	56
WMC (10^5 photons)[a]	79
Convolution	19

[a] Value does not include the convolution time.

emission probability had to be computed only once, the total time for the three spectra was 34 min for the RMC method, compared with 72 h for the standard method. The fluorescence data are presented in two ways, corresponding to the two most common measurement geometries: either full surface illumination and pointwise detection (corresponding to fluorescence imaging) or pointwise illumination and pointwise detection (corresponding to using a single optical fiber for both delivery of excitation light and collection of fluorescence light). The imaging geometry was simulated by recording F_{TOT}, while the fiber geometry was simulated by recording $F_{CW}(r < r_{fiber})$, where r_{fiber} is the radius of the optical fiber. In the example, this was achieved by recording the

signal for only the first spatial grid element. Two of the simulated fluorescence spectra are presented in Fig. 8, together with the intrinsic spectrum for comparison. Only data for the RMC method are shown; the spectra for the other methods were virtually identical. Since the fluorescence quantum yield of PpIX was not known, the spectra were normalized with respect to the peak value for the first case: no photobleaching. In Fig. 9, the relative intensities for the two cases of imaging and fiber detection as the fluorophore was bleached away are presented for the 700-nm simulation.

4. DISCUSSION

Transport theory is frequently used for predicting light propagation and distribution in tissue. However, no analytical solutions exist for the general transport equation. Approximations are required to find such solutions, and many methods have been developed for this purpose. All of them are somehow limited in terms of the geometry and the set of optical properties for which they can provide accurate results. Monte Carlo simulations are considered an accurate method to calculate light propagation in media without restrictions in geometry and optical properties. However, it is a computationally intensive method and does not provide any analytical expression with a functional dependence of parameters of interest. The long computation time is a limitation, especially when modeling tissue fluorescence, since many wavelengths are involved, each influenced by a different set of optical properties and therefore requiring a separate simulation. However, the wide range of optical properties often involved in this type of problem also limits the applicability of the other models developed. In this study, we have developed and demonstrated time-efficient modeling methods for fluorescence in layered tissues based on Monte Carlo simulations with the aim of facilitating the modeling of entire fluorescence spectra. We have further examined the accuracy as well as the gain in computation time provided by these methods.

The SMC method for fluorescence of tissue is essentially adopted from Welch *et al.*[20,21] It is not limited in terms of geometry and is, in this study, assumed to produce accurate results. The results produced with the other methods are thus compared with those from the SMC method. In considering a layered model of the tissue, one can utilize symmetry aspects justifying the method of convolution. Most tissues examined with fluorescence techniques can be considered layered. Thus this assumption cannot be regarded as a severe limitation of the usefulness of the models. There are, in principle, no other assumptions made in the development of this concept, which indicates that the results are as accurate as those for the SMC method. However, the numerical computations may result in a reduced accuracy with use of the convolution technique. This can be attributed to the finite size of the grids of the convolved coordinates. In the SMC simulation, each photon package is tracked from the start until it is terminated or added to the resulting fluorescence function. In the convolution methods, on the other hand, the absorption and emission probabilities are simulated separately. The scores must thus

Table 4. Coefficient of Variation (CV) for the Three Models

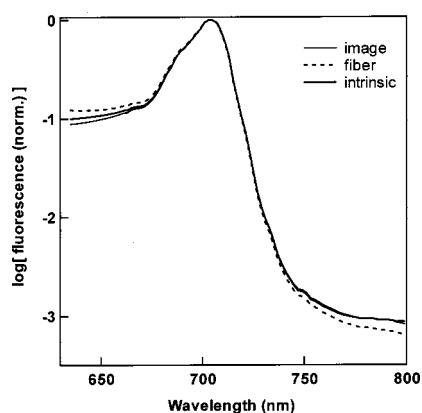| Model	Photons (×1000)	$CV_{10\%}$ (%)	$CV_{1\%}$ (%)	$CV_{0.1\%}$ (%)	CV_{CW} (%)	CV_{TOT} (%)
SMC	1	39	77	104	29	4.3
	4	19	36	56	12	2.3
	16	9.0	18	32	6.2	0.7
	64	5.3	9.7	15	3.3	0.3
	256	2.2	4.4	7.7	1.4	0.3
	1024	1.0	2.1	3.7	0.8	0.2
FMC	1	40	38	41	22	6.6
	4	14	20	23	12	3.2
	16	6.7	9.6	14.1	7.0	1.7
	64	5.1	5.2	7.4	3.3	0.7
	256	2.3	1.9	3.5	1.9	0.2
	1024	0.8	1.0	1.8	0.7	0.2
RMC	1	4.4	6.6	10	7.5	3.4
	4	2.4	3.0	5.1	4.1	1.5
	16	1.2	1.6	2.7	2.4	0.9
	64	0.8	0.9	1.3	0.9	0.2
	256	0.4	0.5	0.8	0.5	0.2
	1024	0.2	0.2	0.3	0.2	0.1

Fig. 8. Simulated fluorescence spectra for PpIX for two different measurement geometries: imaging and direct optical fiber contact. The case of no photobleaching is shown. The intrinsic spectrum used as input is also shown.

be stored as a function of the position and the delay time. The finer the grid size of these coordinates is, the closer the model will imitate the SMC method and the more accurate the results will be. At the same time, a finer grid size will increase the size of the matrices created. This will increase the memory size required, as well as the computation time. The increasing size of the matrices implies longer convolution computations and the need for a larger number of photons launched in order to obtain similar photon statistics for each grid element. This means that there is a trade-off between computation time and accuracy when using convolution. The optimal choice of parameters depends on the optical properties and the geometry of the tissue, as well as on the accuracy required. It is worth noting that the convolution algorithm was not optimized. Replacing the convolution in the spatial and temporal domains with a Fourier transform convolution would increase the speed significantly for larger grid sizes, since the fast Fourier transform

scales as $n \log(n)$, compared with n^2.   In Fig. 5, it was shown that the truncation of the grid used in the accelerated methods caused deviations far from the source, close to the grid boundary. The optimal choice of grid size in terms of minimizing this error would be to extend the grid to the distance where the signal is so low that the statistical noise of the Monte Carlo simulation becomes the dominant error. However, since the convolution is computationally costly, in practice it is better to choose a smaller grid size and accept a small deviation at large distances. The required accuracy for the specific application will have to determine how large a deviation can be tolerated.

In this context, it is also of interest to discuss what accuracy is required in the time domain. In time-resolved fluorescence measurements, the time delay depends on two factors according to Eq. (5)—the time that it takes for the photons to be transported inside the tissue and the fluorescence lifetime of the fluorophore examined. Depending on the fluorescence lifetime, the delay due to the transport will be more or less important. For long fluorescence lifetimes, any deviation in the simulation in the photon path will be smoothed as a result of the convolution with the fluorescence lifetime. Any inaccuracy in the modeling of the temporal behavior of the transport of fluorescence light would thus be less serious. To study the modeling accuracy, we considered a fluorophore with a very short lifetime (1 ps) in all results presented above. The slight systematic difference in F_{TOT} between the SMC method and the accelerated methods, which was seen in Table 2, can be ascribed to an inaccuracy in the convolution method for very early times.

The results clearly show that by separating the calculation of the excitation and escape functions, one can drastically shorten the computation time for Monte Carlo modeling. Of the models suggested in this study, the RMC method is by far the fastest. The results presented in Table 4 show that for $CV_{1\%} \approx 3\%$, the SMC method re-
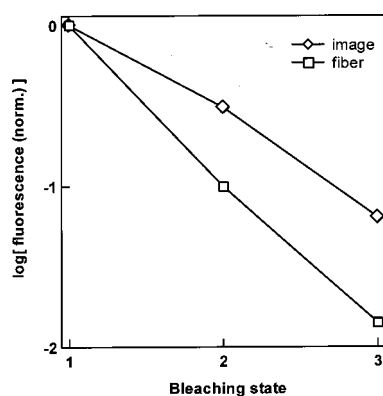
Fig. 9. Relative fluorescence intensity for three different bleaching states and two geometries, imaging (diamonds) and direct optical fiber contact (squares). State 1 corresponds to no bleaching (a 3-mm-thick layer of PpIX) and was used as the reference point. State 2 corresponds to a 2-mm layer of PpIX, starting 1 mm below the surface. In state 3, a 1-mm layer of PpIX located 2 mm below the surface was simulated. The result is shown for the 700-nm simulation.

quires approximately 5×10^5 launched photon packages, while the RMC approach requires as few as 4×10^3, or a reduction of more than 2 orders of magnitude. The corresponding computation times were 6.5 min and 22 s, respectively, where most of the time for the RMC method was used for the convolution. These figures were obtained for the grid size defined in Table 1, used in most of the other calculations presented above. For the integrated quantities, the reduction is less dramatic. To reach $CV_{CW} = 3\%$, the SMC method needed 10^5 photons, while the RMC method required approximately 10^4 photons. For CV_{TOT}, the improvement in the RMC method was even less significant. Thus the great benefits of using the RMC model come when spatially and/or temporally resolved fluorescence simulations are of interest.

With regard to the accuracy of the models, accurate results were obtained from the accelerated modeling in all the functions evaluated, provided that the grid elements were small enough. The FMC and RMC models yielded essentially identical results, which is expected from the theory. A slight, 1% systematic difference between the FMC and RMC methods (see Table 2) can likely be explained by small numerical differences in the algorithms. Because the RMC method is always faster, there is no reason to use the FMC method in practical applications. The usefulness of the FMC method is in demonstrating the concept of convolution to separate the computation of the excitation and escape functions and in that it can be used for validation of the RMC method. It is also worth pointing out that the increased efficiency of the FMC method derives solely from the symmetry of the geometry. For an arbitrary three-dimensional geometry, the FMC method is no more efficient than the SMC method. The RMC method, on the other hand, would still benefit greatly when used under such conditions. Furthermore, the concept of reversed photon paths is not limited to fluorescence problems but can be useful, e.g., when computing photon hitting densities[33] or in any situation where one needs to model a distributed light source and a point detector.[34]

The WMC model can be adapted to any of the above methods. It is not even limited to a layered medium but is valid in general. It has been shown to provide accurate results in previous studies of light propagation in tissue.[24–26] This concept is well suited for the modeling of tissue fluorescence spectra, because of the dependence on the wavelength of the tissue absorption coefficient. One restriction in the utilization of the method to derive a full fluorescence emission spectrum would be that the scattering properties must remain the same in the wavelength region of interest. Since this is a reasonable assumption in a limited wavelength range (e.g., $\Delta\lambda < 50$ nm), fluorescence spectra covering wider spectral ranges can be modeled with a set of separate white simulations, splitting the full range into smaller regions with constant scattering properties. However, for homogeneous nonlayered media, different scattering coefficients can simply be handled by spatially rescaling the emitted fluorescence distribution. This procedure assumes that the anisotropy factor is constant, but such an approximation is often justified in tissues, since the variation in g is usually small over the wavelength region of interest. Also, in the case of diffuse light, only the reduced scattering coefficient $\mu_s' = \mu_s(1 - g)$ is important, and g can be assumed constant.

As an example of the performance of the accelerated models, a realistic situation was modeled, based on fluorescence signals from a photosensitizer used for photodynamic therapy. Three spectra, representing different stages of photobleaching, were simulated. It was shown that a broad fluorescence spectrum could be obtained in as short a time as 20 min, compared with 24 h for the conventional Monte Carlo method. The computation time for the next two spectra was reduced even further thanks to the convolution technique, since the pairs of excitation and emission matrices could be simulated separately, and in this case there was no need to update the emission matrices more than once. The results point once again to the important fact that the scattering and absorption properties of the medium have a decided impact on the fluorescence signal, and there are large differences depending on what type of geometry is used for the measurement. In the region above 635 nm, the absorption in tissue is low and lacks distinguishing spectral features, so there is no large difference in the shape of the spectra for the imaging geometry compared with that for the fiber. However, it is still clear from Fig. 9 that the relative intensities are very different for the two cases of direct-contact fiber and imaging.

The models presented in this work assume that the emitted fluorescence light is collected over the entire hemisphere. However, the collection angle, defined by the numerical aperture of the detector, can have a significant influence on the signal.[35] It should be noted that this was not considered in the example of PpIX fluorescence. In the Monte Carlo models, defining the collection angle of the recorded light could fairly easily be implemented, since this information is available for each photon that escapes the medium. The difference for the accelerated models is that the emission probability has to be computed for the specific collection angle of the detector. For the RMC method, this would mean that the solid

angle of emission, $\Delta\Omega$, for the source in Eq. (11) would instead be defined by Snell's law and the desired emittance angle above the surface.

In conclusion, several approaches to increase the speed of Monte Carlo simulations for modeling of the fluorescence of layered tissues are presented. The method of convolution can be used in combination with Monte Carlo simulations to separate the computation of the excitation and emission light profiles. We further suggest that with use of the reciprocity relation between a forward and a reversed photon path in the medium, the efficiency of the calculation of the emission probability increases dramatically. The computation time for this reverse-emission Monte Carlo method was up to 2 orders of magnitude faster than that for the standard fluorescence Monte Carlo method. The use of the white Monte Carlo approach is especially well suited for modeling fluorescence emission spectra in tissue. For a homogeneous medium, where the scattering anisotropy factor is independent of the wavelength in the region of interest, in principle only one simulation is needed to solve the entire problem by scaling of the scattering coefficient. Even if a set of simulations is necessary for each wavelength band, the reverse-emission approach yields a significant reduction in computation time.

ACKNOWLEDGMENTS

Corresponding author Johannes Swartling can be reached by e-mail: johannes.swartling@fysik.lth.se.

REFERENCES

1. I. J. Bigio and J. R. Mourant, "Ultraviolet and visible spectroscopies for tissue diagnostics: fluorescence spectroscopy and elastic-scattering spectroscopy," Phys. Med. Biol. **42**, 803–814 (1997).
2. G. A. Wagnières, W. M. Star, and B. C. Wilson, "*In vivo* fluorescence spectroscopy and imaging for oncological applications," Photochem. Photobiol. **68**, 603–632 (1998).
3. N. Ramanujam, J. Chen, K. Gossage, R. Richards-Kortum, and B. Chance, "Fast and noninvasive fluorescence imaging of biological tissues *in vivo* using a flying-spot scanner," IEEE Trans. Biomed. Eng. **48**, 1034–1041 (2001).
4. D. Y. Paithankar, A. U. Chen, B. W. Pogue, M. S. Patterson, and E. M. Sevick-Muraca, "Imaging of fluorescent yield and lifetime from multiply scattered light reemitted from random media," Appl. Opt. **36**, 2260–2272 (1997).
5. J. M. Still, E. J. Law, K. G. Klavuhn, T. C. Island, and J. Z. Holtz, "Diagnosis of burn depth using laser-induced indocyanine green fluorescence: a preliminary clinical trial," Burns **27**, 364–371 (2001).
6. R. Weissleder, C.-H. Tung, U. Mahmood, and A. Bogdanov, "In vivo imaging of tumors with protease-activated near-infrared fluorescent probes," Nat. Biotechnol. **17**, 375–378 (1999).
7. M. Canpolat and J. R. Mourant, "Monitoring photosensitizer concentration by use of a fiber-optic probe with a small source-detector separation," Appl. Opt. **39**, 6508–6514 (2000).
8. M. Sinaasappel and H. J. C. M. Sterenborg, "Quantification of the hematoporphyrin derivative by fluorescence measurement using dual-wavelength excitation and dual-wavelength detection," Appl. Opt. **32**, 541–548 (1993).
9. H. J. C. M. Sterenborg, A. E. Saarnak, R. Frank, and M. Motamedi, "Evaluation of spectral correction techniques for fluorescence measurements on pigmented lesions in vivo," J. Photochem. Photobiol. B **35**, 159–165 (1996).
10. J. Wu, M. S. Feld, and R. P. Rava, "Analytical model for extracting intrinsic fluorescence in turbid media," Appl. Opt. **32**, 3585–3595 (1993).
11. S. Warren, K. Pope, Y. Yazdi, A. J. Welch, S. Thomsen, A. L. Johnston, M. J. Davis, and R. Richards-Kortum, "Combined ultrasound and fluorescence spectroscopy for physicochemical imaging of atherosclerosis," IEEE Trans. Biomed. Eng. **42**, 121–132 (1995).
12. C. M. Gardner, S. L. Jacques, and A. J. Welch, "Fluorescence spectroscopy of tissue: recovery of intrinsic fluorescence from measured fluorescence," Appl. Opt. **35**, 1780–1792 (1996).
13. M. G. Muller, I. Georgakoudi, Q. Zhang, J. Wu, and M. S. Feld, "Intrinsic fluorescence spectroscopy in turbid media: disentangling effects of scattering and absorption," Appl. Opt. **40**, 4633–4646 (2001).
14. M. S. Patterson, S. Andersson-Engels, B. C. Wilson, and E. K. Osei, "Absorption spectroscopy in tissue-simulating materials: a theoretical and experimental study of photon paths," Appl. Opt. **34**, 22–30 (1995).
15. M. S. Patterson and B. W. Pogue, "Mathematical model for time-resolved and frequency-domain fluorescence spectroscopy in biological tissues," Appl. Opt. **33**, 1963–1974 (1994).
16. R. Richards-Kortum, R. P. Rava, R. Cothren, A. Metha, M. Fitzmaurice, N. B. Ratliff, J. R. Kramers, C. Kittrell, and M. S. Feld, "A model for extraction of diagnostic information from laser induced fluorescence spectra of human artery wall," Spectrochim. Acta Part A **45**, 87–93 (1989).
17. A. H. Gandjbakhche, R. F. Bonner, R. Nossal, and G. H. Weiss, "Effects of multiple-passage probabilities on fluorescent signals from biological media," Appl. Opt. **36**, 4613–4619 (1997).
18. M. Keijzer, S. L. Jacques, S. A. Prahl, and A. J. Welch, "Light distribution in artery tissue: Monte Carlo simulations for finite-diameter laser beams," Lasers Surg. Med. **9**, 148–154 (1989).
19. C. M. Gardner and A. J. Welch, "Monte Carlo simulation of light transport in tissue: unscattered absorption events," Appl. Opt. **33**, 2743–2745 (1994).
20. A. J. Welch and R. Richards-Kortum, "Monte Carlo simulation of the propagation of fluorescent light," in *Laser-induced Interstitial Thermotherapy*, G. Müller and A. Roggan, eds. (Society of Photo-Optical Instrumentation Engineers, Bellingham, Wash., 1995), pp. 174–189.
21. A. J. Welch, C. M. Gardner, R. Richards-Kortum, E. Chan, G. Criswell, J. Pfefer, and S. Warren, "Propagation of fluorescence light," Lasers Surg. Med. **21**, 166–178 (1997).
22. R. J. Crilly, W. F. Cheong, B. Wilson, and J. R. Spears, "Forward-adjoint fluorescence model: Monte Carlo integration and experimental validation," Appl. Opt. **36**, 6513–6519 (1997).
23. S. Avrillier, E. Tinet, D. Ettori, J.-M. Tualle, and B. Gélébart, "Influence of the emission-reception geometry in laser-induced fluorescence spectra from turbid media," Appl. Opt. **37**, 2781–2787 (1998).
24. A. Pifferi, R. Berg, P. Taroni, and S. Andersson-Engels, "Fitting of time-resolved reflectance curves with a Monte Carlo model," in *Advances in Optical Imaging and Photon Migration*, R. R. Alfano and J. G. Fujimoto, eds., Vol. 2 of OSA Trends in Optics and Photonics Series (Optical Society of America, Washington, D.C., 1996), pp. 311–314.
25. A. Kienle and M. S. Patterson, "Determination of the optical properties of turbid media from a single Monte Carlo simulation," Phys. Med. Biol. **41**, 2221–2227 (1996).
26. A. Pifferi, P. Taroni, G. Valentini, and S. Andersson-Engels, "Real-time method for fitting time-resolved reflectance and

transmittance measurements with a Monte Carlo model," Appl. Opt. **37**, 2774–2780 (1998).

27. L. Wang, S. L. Jacques, and L. Zheng, "MCML—Monte Carlo modeling of light transport in multi-layered tissues," Comput. Methods Programs Biomed. **47**, 131–146 (1995).

28. S. Andersson-Engels, A. M. K. Enejder, J. Swartling, and A. Pifferi, "Accelerated Monte Carlo models to simulate fluorescence of layered tissue," in *Photon Migration, Diffuse Spectroscopy, and Optical Coherence Tomography: Imaging and Functional Assessment*, S. Andersson-Engels and J. G. Fujimoto, eds., Proc. SPIE **4160**, 14–15 (2000).

29. K. M. Case and P. F. Zweifel, *Linear Transport Theory* (Addison-Wesley, Reading, Mass., 1967).

30. H. R. Gordon, "Equivalence of the point and beam spread functions of scattering media: a formal demonstration," Appl. Opt. **33**, 1120–1122 (1994).

31. R. Berg, "Laser-based cancer diagnostics and therapy— tissue optics considerations," Ph.D. thesis (Lund Institute of Technology, Lund, Sweden, 1995).

32. A. J. Welch and M. J. C. van Gemert, *Optical-Thermal Response of Laser-Irradiated Tissue* (Plenum, New York, 1995).

33. S. R. Arridge and M. Schweiger, "Photon-measurement density functions. Part 2: Finite-element-method calculations," Appl. Opt. **34**, 8026–8037 (1995).

34. P. Weibring, J. Swartling, H. Edner, S. Svanberg, T. Caltabiano, D. Condarelli, G. Cecchi, and L. Pantani, "Optical monitoring of volcanic sulphur dioxide emissions— comparison between four different remote-sensing spectroscopic techniques," Opt. Lasers Eng. **37**, 267–284 (2002).

35. T. J. Pfefer, K. T. Schomacker, M. N. Ediger, and N. S. Nishioka, "Light propagation in tissue during fluorescence spectroscopy with single-fiber probes," IEEE J. Sel. Top. Quantum Electron. **7**, 1004–1012 (2001).